

# Detection and Analysis of Edge Localised Modes in Tokamak Plasmas

Tobias Schuett

*Department of Physics, University of York, UK*

Submitted in May 2021

## Abstract

This thesis presents methods to detect edge localised modes (ELMs) in tokamak plasmas and uses these for the analysis of ELM characteristics. ELMs are plasma eruptions at the outer edge of tokamak plasmas that exert large heat loads on the plasma facing components. Two detection mechanisms were developed in the gas puff imaging (GPI) and outer divertor current (Ipolsola) diagnostics and their accuracy tested, showing lowest false positive rates of  $\sim 3\%$  in the GPI and  $\sim 4\%$  in the Ipolsola. Using these mechanisms the temporal ELM shape was averaged over 144 (GPI) and 163 ELMs (Ipolsola). The coefficient of variation of the ELM period of 36% (GPI) and 29% (Ipolsola) confirms the quasi-periodicity of the ELMs described in literature. Finally, an apparent time offset between the two diagnostics signals was investigated, showing not to be of physical nature but rather a mismatch in the involved clocks.

# Contents

	page
<b>1 Introduction</b>	<b>1</b>
<b>2 Methods</b>	<b>4</b>
2.1 Background . . . . .	4
2.1.1 Diagnostics . . . . .	4
2.1.2 Plasma q-value . . . . .	5
2.1.3 Plasma Sound Speed . . . . .	6
2.2 Detection Mechanisms . . . . .	7
2.2.1 Coding Environment . . . . .	7
2.2.2 ELM Frequency . . . . .	7
2.2.3 Mechanism 1 . . . . .	8
2.2.4 Mechanism 2 . . . . .	11
2.2.5 Parameter Optimisation . . . . .	12
2.2.6 Combining Mechanisms . . . . .	13
<b>3 Results and Discussion</b>	<b>13</b>
3.1 Detection Mechanism Performance . . . . .	13
3.2 ELM Characteristics . . . . .	16
3.2.1 Temporal Shape . . . . .	16
3.2.2 Ipolsola and GPI Offset . . . . .	19
3.2.3 ELM Frequency & Periodicity . . . . .	21
<b>4 Conclusion</b>	<b>23</b>
<b>Appendices</b>	<b>24</b>
<b>A Python Code</b>	<b>24</b>
<b>B Uniform Distribution</b>	<b>24</b>
<b>References</b>	<b>25</b>

## 1 Introduction

When deuterium and tritium are fusing together to form an alpha particle, a neutron and excess energy of 17.6 MeV are released in the process [1]. In order for fusion to take place the two nuclei must overcome each other's Coulomb barrier to enter the range of nuclear separation where the strong nuclear force is dominant. One method to achieve this is to heat up the deuterium and tritium until their thermal energies are large enough to overcome their Cou-

lomb barriers. This process is called thermonuclear fusion and requires mean temperatures of  $k_B T = 10$  keV [2]. At these temperatures and sufficiently high plasma densities, the deuterium and tritium atoms are fully ionised, defining a new class of gases called plasma [3]. Due to the high temperatures of the plasma, it is not possible to confine the plasma within material walls. A tokamak reactor, that has the shape of a torus, confines the plasma using a combination of strong poloidal and toroidal magnetic fields without the plasma coming into contact with the material walls [1].

Even though the plasma's net electric charge is neutral, it consists of an equal amount of positively charged ions and free electrons. Hence, the plasma dynamics are mostly due to the electromagnetic interaction between the particles and with the external magnetic field [3]. The strong toroidal magnetic field allows for high velocities of the plasma particles along the magnetic field lines, but restricts the radial motion to a gyrating motion and drift velocities of much smaller magnitudes and therefore confines the plasma in a toroidal shape [3]. The drift velocities are of opposite direction for ions and electrons, leading to unwanted charge separation. Hence, a toroidal plasma current is induced by transformer coils located in the centre of the torus. This plasma current produces a poloidal magnetic field which combined with the externally applied toroidal magnetic field results in helical magnetic field lines that hinder charge separation and improve the confinement. The external toroidal field is typically in the order of a few teslas, whereas the poloidal field is usually an order of magnitude smaller and associated with a plasma current in the MA range [1, 2]. The helical field lines create closed magnetic flux surfaces that contain the plasma. The last closed flux surface (LCFS), also described as the separatrix, describes the boundary between the core plasma and the so called scrape-off layer (SOL) [4]. The SOL is the region at the outer edge of the tokamak where the magnetic field lines are open. Thus, they are not forming closed surfaces but instead reach plasma facing components as seen in figure 2. The SOL is characterised by its low temperature and low plasma density compared to the core plasma [4].

There are two fundamentally different approaches to understanding the plasma dynamics in an electromagnetic field. One deriving the overall plasma behaviour from the single-particle motion in an externally applied electric and magnetic field. This approach is valid for plasmas of low densities where the interaction between the plasma particles can be mostly neglected [3]. When studying slow and large scale phenomena in high density and high temperature plasmas that are confined by strong magnetic fields as present in a tokamak, it becomes more useful to use statistical methods by introducing a particle distribution function  $f(\vec{r}, \vec{v}, t)$  and to treat the plasma as a single fluid. This approach is called magnetohydrodynamics (MHD) [3]. Edge localised modes (ELMs) are an MHD instability that become apparent when the tokamak has transitioned to the high confinement regime (H-mode) [5]. Whereas the low

confinement regime (L-mode) is characterised by a comparatively low temperature gradient and significant particle transport through the LCFS, the H-mode is achieved by an increase in plasma heating power and leads to the development of an edge transport barrier (ETB) just inside the LCFS [4, 6]. The ETB is characterised by high gradients in both plasma density and temperature [7].

The rising temperature gradient results in an ELM instability where plasma eruptions are transported into the SOL of the tokamak and then follow the helical magnetic field lines to the divertor and other plasma facing components (PFC) at the outer edge of the tokamak. The ELM instability leads to a decrease in the density and temperature gradients of the ETB which then build up until the next ELM instability is triggered [7].

An intrinsic feature of H-mode is the confinement of fuel-ions and impurities in the core plasma [7]. This is caused by the ETB as it prevents particle transport from the core plasma to the SOL. The impurities lead to radiative energy loss due to bremsstrahlung arising from the interaction of plasma particles with high Z (atomic number) impurities. ELMs are helpful in this regard as they help to transport impurities out of the core plasma through the ETB into the SOL [7].

However, due to the short ELM duration of  $\sim 200 \mu\text{s}$  [8] the high heat flux can result in damage to PFCs and diagnostics in future large tokamaks such as ITER [7]. The energy of each ELM and the associated heat load can be reduced by increasing the ELM frequency (ELM mitigation) or by finding mechanisms to prevent ELM instabilities (ELM suppression) [9].

Both ELM mitigation and ELM suppression require a better understanding of ELMs for which detection methods and knowledge of their characteristics are needed. A key challenge in detecting ELMs is their different shapes and quasi-periodicity.

Section 2.1 describes the diagnostics in which the detection and analysis of the ELMs takes place and introduces additional plasma parameters, while section 2.2 describes the working principles of the two mechanisms that were developed to detect the ELMs. The first part of the results 3.1 analyses the detection accuracy of the mechanisms. The second part 3.2 analyses the temporal shape of an ELM, their periodicity and a time offset that was found between the GPI and Ipolsola data.

## 2 Methods

### 2.1 Background

#### 2.1.1 Diagnostics

Gas puff imaging (GPI), being one of the diagnostics used in this report to detect and analyse ELMs, uses neutral gas injection of deuterium or helium to observe the plasma density in the SOL [10]. As the neutral background density is increased by the gas puff, the collision with plasma particles leads to spontaneous emission. In the ASDEX Upgrade tokamak (AUG) the resulting photons are detected by a fast camera with a  $64 \times 64$  px spatial resolution and a  $5 \mu\text{s}$  frame rate.

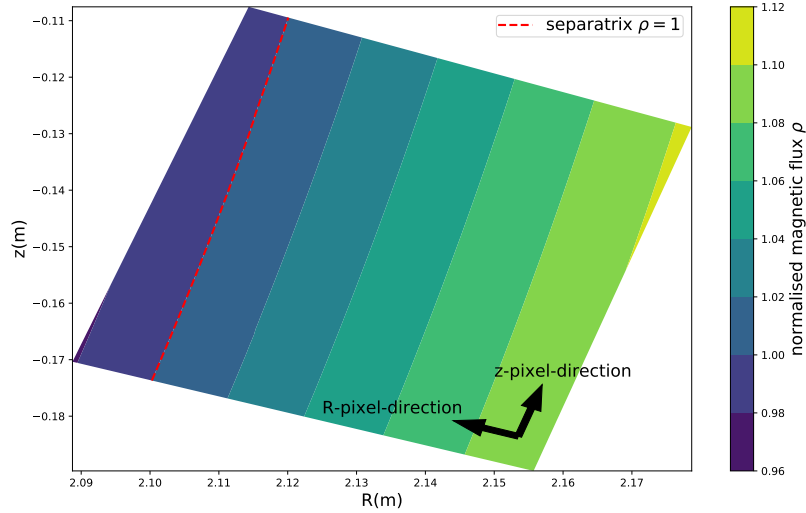


Figure 1: The magnetic flux parameter  $\rho$  at each location of the GPI diagnostic normalised by the magnetic flux at the LCFS. Also shown are the direction of the R-pixel and the z-pixel axes.

The area covered by the fast camera is shown in figure 1. The magnetic flux parameter  $\rho$  describes the position of each pixel within the magnetic field of the tokamak. Figure 1 shows the LCFS in red. Hence, the majority of the area covered by the GPI is located in the SOL. It is important to distinguish between the location with R and z given in meters and the one given in pixels as often used in this report. The location in pixel space corresponds to the layers in the data arrays and also has the advantage that z-pixels for a given R-pixel have similar magnetic flux values. The location of the GPI within AUG is shown in black in figure 2. The experimental data is generally divided into

different shots of a few seconds in length. Each of the shots contains multiple intervals of lengths  $\sim 0.2\text{s}$  where the neutral gas puff is active. In this thesis these intervals are used for the GPI and the Ipolsola in order to be able to compare the signal between the two diagnostics.

Ipolsola, being the second diagnostic used in this report, is the average of several shunt currents measured in the divertor region of the tokamak [11]. The currents are being measured at different locations in the divertor tiles of the tokamak as shown in figure 2. The name Ipolsola describes the fact that this signal “corresponds to the poloidal SOL current measurement in the outer (außen) divertor” [11, p.49].

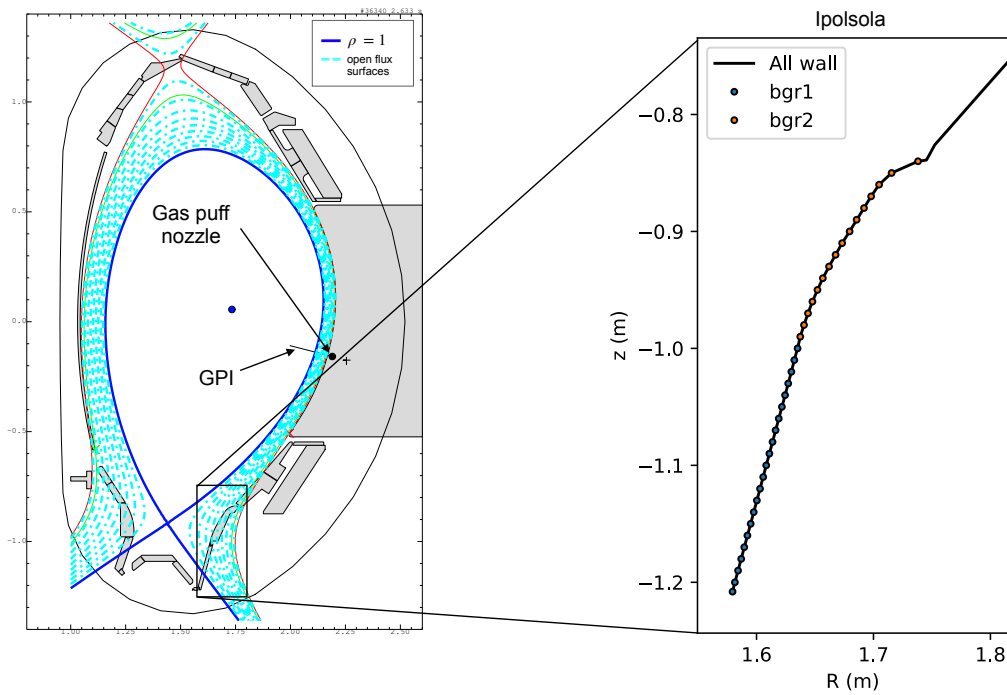


Figure 2: Left: The AUG dimensions with the separatrix, i.e.  $\rho = 1$ , in dark blue, the open magnetic flux surfaces in light blue and the GPI location in black. Right: The origin of the Ipolsola data of the 2 divertor tiles “baugruppe 1” in blue and “baugruppe 2” in orange.

### 2.1.2 Plasma q-value

The position within a tokamak is often given in terms of the major radius  $R$  or the minor radius  $r$  as seen in figure 3.

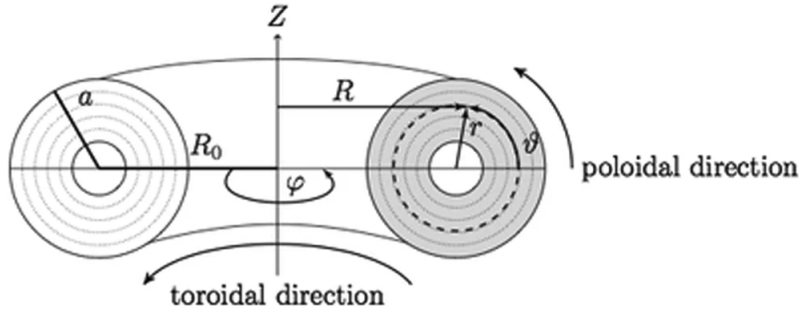


Figure 3: The coordinate system typically used to describe the location within a tokamak. Image taken from [12].

An important characteristic of a magnetically confined fusion configuration is its safety factor which is generally defined as the inverse of the rotational transform  $\iota$

$$q \equiv \frac{2\pi}{\iota} \quad (1)$$

where the rotational transform is given as the change in the poloidal angle  $\vartheta$  after a full toroidal transit of the helical formed magnetic field lanes:

$$\iota(r) \equiv \Delta\vartheta(r) = \vartheta(\varphi + 2\pi) - \vartheta(\varphi) \quad (2)$$

with the toroidal angle  $\varphi$  and the tokamak major radius  $R$  [1, pp.286-287]. When approximating the torus as a cylinder this becomes:

$$\iota(r) \approx 2\pi \frac{RB_p(r)}{rB_t(r)} \quad (3)$$

with the poloidal magnetic field  $B_p$  and the toroidal magnetic field  $B_t$ . Hence, the safety factor is given by [1]

$$q(r) = \frac{2\pi}{\Delta\vartheta(r)} \approx \frac{rB_t(r)}{RB_p(r)} \quad (4)$$

The first step of equation 4 best illustrates that the q-value can be understood as a measure of how many toroidal transits of the magnetic field lanes are necessary in order to achieve a full poloidal transit, i.e.  $\vartheta = 2\pi$ . The name safety factor originates from the fact that plasmas with larger q-values are more stable against MHD instabilities [1]. An often used q-value is  $q_{95}$  which represents the q-value at 95% of the magnetic flux [13, 14].

### 2.1.3 Plasma Sound Speed

The speed of sound in a fluid is generally given by the Newton-Laplace equation [15]:

$$C_s = \sqrt{B/\rho} \quad (5)$$

with the bulk modulus  $B$  and fluid density  $\rho$ . The bulk modulus  $B$  is generally given by [16, p.535]:

$$B = -V \frac{dp}{dV} \quad (6)$$

On the length scale that the sound waves propagate it is valid to treat the plasma as an ideal gas whose inertia is mainly given by the plasma ions ( $m_i \gg m_e$ ) [3, p.190]. In this approximation the fluid density becomes:

$$\rho = n_i m_i \quad (7)$$

By using the ideal gas law  $pV = Nk_B T$  and assuming a constant plasma temperature, i.e.  $pV = \text{const}$ , the bulk modulus is then given by:

$$B_T = -V \frac{d}{dV} \left( \frac{N_i k_B T}{V} \right) = n_i k_B T \quad (8)$$

where  $k_B$  is the Boltzmann constant. Hence, by using equation 5 the ion speed of sound is given by:

$$C_s = \sqrt{\frac{n_i k_B T}{n_i m_i}} = \sqrt{\frac{2k_B T}{5m_p}} \quad (9)$$

where the ion mass  $m_i = 5m_p/2$  is approximated by the mean of the deuterium ion mass of  $\sim 2m_p$  and tritium ion mass of  $\sim 3m_p$ , where  $m_p$  is the proton mass.

## 2.2 Detection Mechanisms

### 2.2.1 Coding Environment

The coding for detecting and analysing the ELMs was done in Python 3 using the *Jupyter Notebook* environment. For standard functions and operations the libraries NumPy [17], Matplotlib [18] and SciPy [19] were used. See appendix A for an interactive version of this thesis that contains the python code.

### 2.2.2 ELM Frequency

A mechanism was developed to assign one frequency  $f_{\text{ELM}}$  to a given time history of the GPI or Ipolsola data. This was done by setting the frequency that corresponds to the peak in the power spectrum of the signal as the ELM frequency. The power spectrum was calculated by taking the Fourier transform of the autocorrelation function (ACF) of the signal [20, p.94]. The idea was that the ELM frequency is the most dominant frequency in the ACF. The discrete autocorrelation function of the discrete real function  $s[t]$  is given by

$$\text{ACF}(s[t])(\tau) = \sum_{t=0}^{n-1} s[t + \tau] * s[t] \quad (10)$$



$\tau$  was chosen to run between  $[-\frac{n-1}{2}, \frac{n-1}{2}]$  for odd  $n$  and between  $[-\frac{n}{2}, \frac{n}{2} - 1]$  for even  $n$  such that the resulting function has a length of  $n$ . Note that any terms where one of the indices runs outside the range of  $s[t]$  is set to zero.

The discrete Fourier transform (DFT) of the ACF is given by:

$$s[k] = \sum_{\tau=0}^{n-1} \text{ACF}[\tau] \exp \left\{ -i2\pi \frac{k}{n} \tau \right\} \quad (11)$$

where  $k=0, \dots, n-1$ .

### 2.2.3 Mechanism 1

In a first preparational step the GPI signal is averaged along the  $z$ -pixel-direction for each pixel in  $R$ -pixel-direction. For this all pixels are included which have an average brightness  $I(R, z) > 0.9 \cdot I(R, \max I_z)$  as seen in figure 4, where  $(\max I_R, \max I_z)$  corresponds to the overall brightest pixel during one shot.

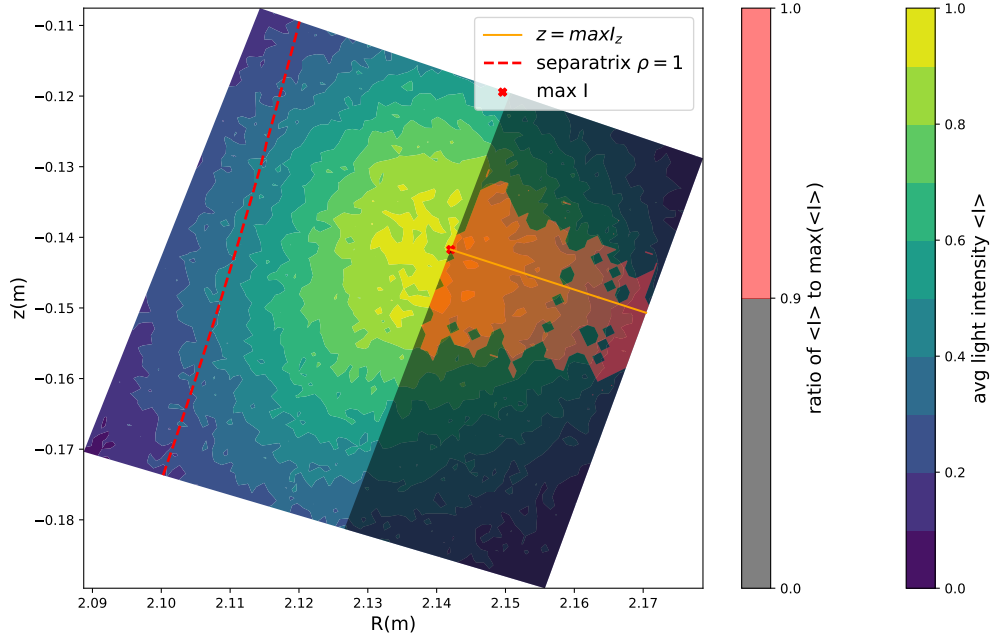


Figure 4: The included pixels for the averaging along the  $z$ -pixel-direction for each  $R > \max I_R$  pixel of the GPI diagnostics shaded in red.

The averaging shows to result in a reduction of noise and does not result in a smearing of the signal. The averaging condition imposed on the brightness of the pixels prevents a mixing of ELMy with non-ELMy data. For detecting

the ELMs and analysing their average shape in the GPI, the averaged signal at  $R = 55$  px was chosen. At this location the ratio between the neutral gas density  $n_{neutral}$  and the plasma background density  $n_e$  is high as it is located further away from the separatrix and core plasma but closer to the neutral gas source. This results in clearly visible positive peaks in brightness produced by ELMs.

The first ELM detection mechanism operates on the first time derivative of the averaged GPI signal in order to detect the ELMs. It uses the fact that the first time derivative shows to have generally higher values immediately after an ELM occurred as can be seen in figure 5. The first time derivative was calculated by applying the NumPy gradient function along the time axis of the signal [17]. In the Ipolsola this mechanism works directly on the signal as its time series is similar to the time derivative of the GPI signal. In the first

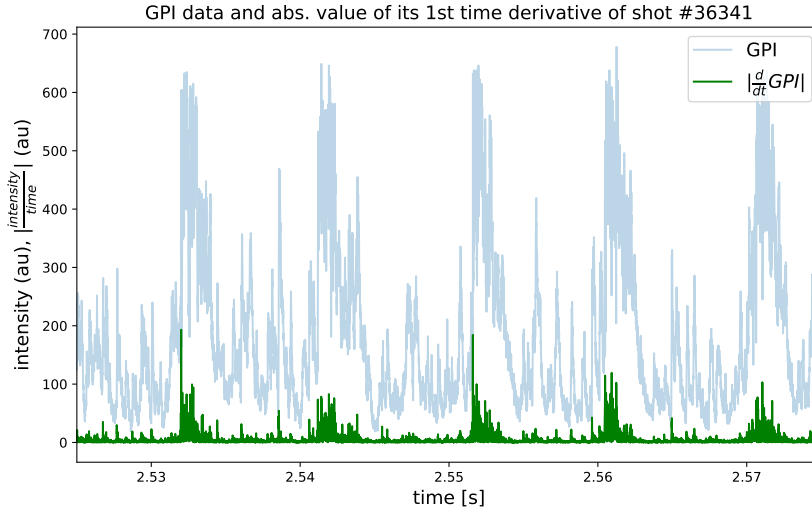


Figure 5: The first time derivative of the averaged GPI signal @R=55px.

step a moving average (MA) with a boxcar length of  $\Delta t = 500 \mu s$  is created

$$MA[t] = \sum_{n=0}^{\Delta t} s[t - n] \quad (12)$$

with  $s[t]$  being the time derivative of the GPI signal or the original Ipolsola signal. This is then used to compute the forward difference  $f[t]$  [21, p.182]:

$$f[t] = MA[t + \Delta t] - MA[t] \quad (13)$$

Note that MA is computed backwards such that  $f$  is centred on  $t$ . The idea here is that a local maximum of  $f$  means that this point corresponds to the start of an ELM. The normalised output of this step is shown in figure 6.

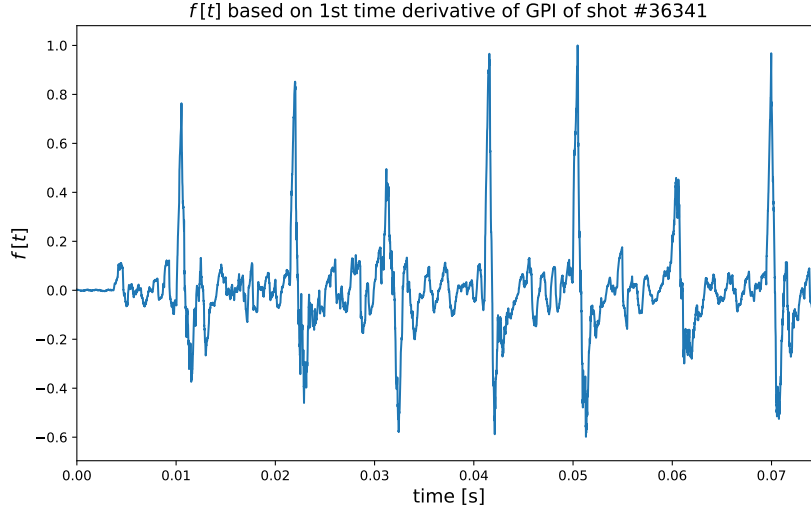


Figure 6: The normalised forward difference  $f$  defined in equation 13 plotted for a segment of the GPI data of #36341 and normalised by the maximum of  $f$ .

An additional parameter of the algorithm is introduced that will be referred to as the *flagging threshold*. This parameter is necessary to decide which of the peaks visible in figure 6 will be accepted as an ELM by requiring a minimum height for a peak:

$$f_2 = \begin{cases} f[t] & \text{for } f[t] > \text{threshold} \\ 0 & \text{for } f[t] \leq \text{threshold} \end{cases} \quad (14)$$

In the next step, the algorithm would search for local maxima of  $f_2$  by determining the maxima within each time interval during which all data points are consistently different from zero (referred to as *search intervals*):

$$\max(f_2[t]) = f_2[t_{ELM}] \quad (15)$$

where  $t$  runs only within the  $i$ -th search interval  $t \in [t_i^{\text{start}}, t_i^{\text{final}}]$ .

However, by applying the *flagging threshold* to  $f$  there is occasionally more than one search interval within one larger peak that seems to be caused by the same ELM. This phenomenon is displayed in figure 7 and stems from the sharp character of the threshold. Small fluctuations of  $f$  around the threshold will cause multiple search intervals.

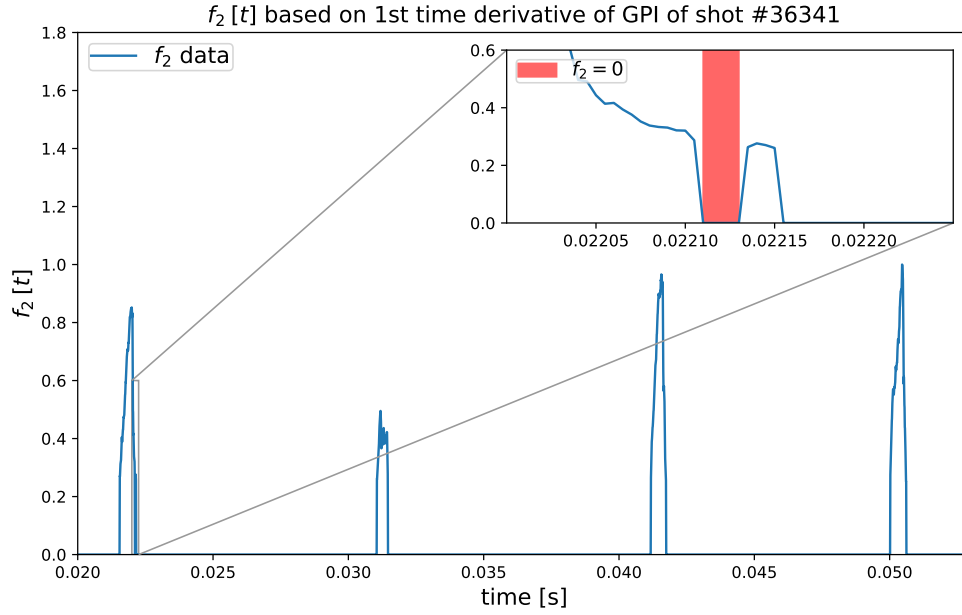


Figure 7: The function  $f_2$  defined in equation 14 for a segment of the GPI data of #36341.

To correct for this, a second parameter is introduced that will be referred to as the *flagging delta*, which allows to merge some search intervals together into larger *valid intervals*.

A search interval's start time is only a start time for a valid interval if the start time of the last valid interval is further away than *flagging delta* (by definition the start time of the first search interval is a valid start time). Identifying a new valid interval's start time as the start time of the  $i$ -th search interval allows to determine the final time of the last valid interval as the final time of the last search interval  $i - 1$ .

In a final step the maximum of each valid interval is determined and the associated time saved as the start of one ELM.

#### 2.2.4 Mechanism 2

This mechanism makes use of the cross-correlation<sup>1</sup> of the GPI signal and the time series of a single ELM. Let  $s[t]$  be the GPI signal and  $g[t]$  the shorter time series of a single ELM region of length  $\Delta t = 4.5$  ms.  $g$  was chosen manually as an average sized ELM. The length  $\Delta t$  is chosen as such to contain the section of increased intensity around an ELM. The ELM region sample  $g[t]$  has a labelled

<sup>1</sup>Note that compared to the convolution of  $s$  and  $g$ , the cross-correlation does not flip  $g$  before computing the overlap with  $s$ .

ELM start time at  $t_{sample}^{ELM}$ . The discrete cross-correlation is then defined as:

$$c[\tau] = g[t] * s[t] = \sum_{t=0}^{\Delta t} g[\tau + t] \cdot s[t] \quad (16)$$

The idea is that  $c[\tau]$  will have higher values for shift times  $\tau$  where  $s$  has a similar shape to  $g$ .  $c$  generally shows no clear change for different  $g$  as long as  $g$  is chosen as the same type of ELM [5, p.107]. The output of this step can be seen in figure 8.

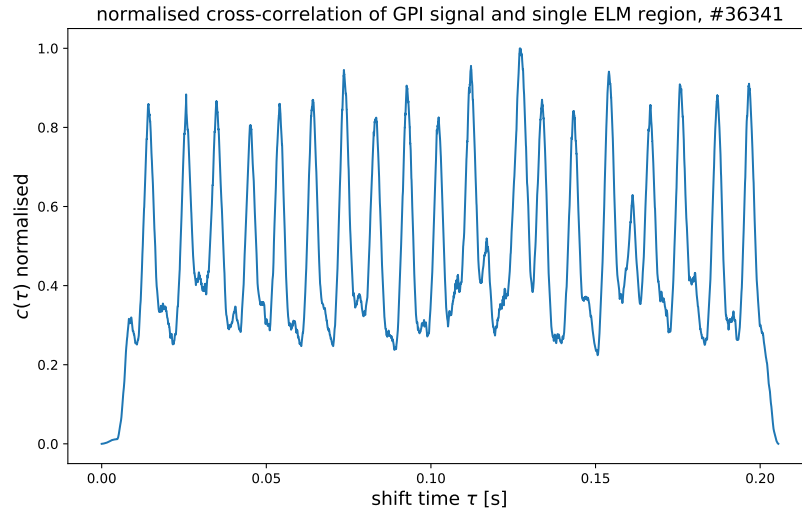


Figure 8: The normalised cross-correlation  $c[\tau]$  as defined in equation 16 for a segment of shot #36341.

The local maxima will then respond to the best overlap between both signals. The location of the ELM in  $s[t]$  can be calculated as:

$$t_i^{ELM} = \tau_i^{ELM} + t_{sample}^{ELM} \quad (17)$$

where  $\tau = 0$  corresponds to the first complete overlap of both  $s$  and  $g$ . As  $c[\tau]$  has a similar shape as the function  $f$  of Mechanism 1 in figure 6 of section 2.2.3, the remainder of this algorithm works analogous to Mechanism 1 with the use of a *flagging threshold* and a *flagging delta*. Note however, that generally the optimal values for these parameters will be different for both mechanisms.

### 2.2.5 Parameter Optimisation

The goal of this step is to find the values of the *flagging threshold* and *flagging delta* for each mechanism which result in the highest detection efficiency. In order to find the optimal values, ELM labels were created for two gas puffs of

the GPI diagnostic. This corresponds to 56 labelled ELMs during  $\sim 0.4$  s. In the next step a loss function  $L$  is defined which assigns a real number to each parameter pair of *flagging threshold* (thres) and *flagging delta* (fdelta):

$$L(\text{thres}, \text{fdelta}) = fn(\text{thres}, \text{fdelta}) + fp(\text{thres}, \text{fdelta}) \quad (18)$$

with the false negative rate defined as:

$$fn = \frac{FN}{FN + TP} \quad (19)$$

and the modified false positive rate:

$$fp = \frac{FP}{FP + TP} \quad (20)$$

with FP, FN and TP being the number of false positives, false negatives and true positives detected ELMs (flags), respectively. In a next step,  $L$  was evaluated for a range of both parameters to determine the parameter values with minimal loss values. A labelled ELM was counted as being correctly detected if the flag raised by the mechanism lies within an interval of  $\pm 1$  ms of the label. It showed that flags within this region seem to refer to the same ELM.

### 2.2.6 Combining Mechanisms

In a final step, mechanism 1 (M1) of section 2.2.3 and mechanism 2 (M2) of section 2.2.4 were combined for both the GPI and the Ipolsola diagnostic. This combined mechanism (CM) allows to produce a single output of detected ELMs each assigned with a degree of confidence indicating whether the detection is based on both mechanisms, M1 only or M2 only. As in section 2.2.5 two flags of both algorithms were accepted as referring to the same ELM if they are less than 1 ms apart from each other.

## 3 Results and Discussion

### 3.1 Detection Mechanism Performance

The optimisation mechanism described in section 2.2.5 results in the following optimal parameters for detection mechanisms M1 and M2.

#36341 - GPI	Mechanism 1	Mechanism 2
optimal flagging threshold	0.27	0.51
optimal flagging delta [ms]	1.3	1.2
#36341 - Ipolsola	Mechanism 1	Mechanism 2
optimal flagging threshold	0.18	0.13
optimal flagging delta [ms]	1.45	0.45

Table 1: The optimal parameters for Mechanism 1 and 2 for the GPI (top) and Ipolsola (bottom) diagnostic for the labelled shot #36341.

These parameters result in the following false positive rates, false negative rates and associated loss function values.

#36341 - GPI	Mechanism 1	Mechanism 2	Combi Mechanism
$fp(\text{thres}, \text{fdelta})$ [%]	11.69	4	2.38
$fn(\text{thres}, \text{fdelta})$ [%]	9.52	17.14	23.81
$L(\text{thres}, \text{fdelta})$ [%]	<b>21.21</b>	<b>21.14</b>	<b>26.19</b>
#36341 - Ipolsola	Mechanism 1	Mechanism 2	Combi Mechanism
$fp(\text{thres}, \text{fdelta})$ [%]	4.17	3.23	3.45
$fn(\text{thres}, \text{fdelta})$ [%]	2.86	8.57	11.43
$L(\text{thres}, \text{fdelta})$ [%]	<b>7.03</b>	<b>11.8</b>	<b>14.88</b>

Table 2: The false positive rates, false negative rates and loss function  $L$  values for M1 and M2 being run with optimal parameters on the GPI and Ipolsola.

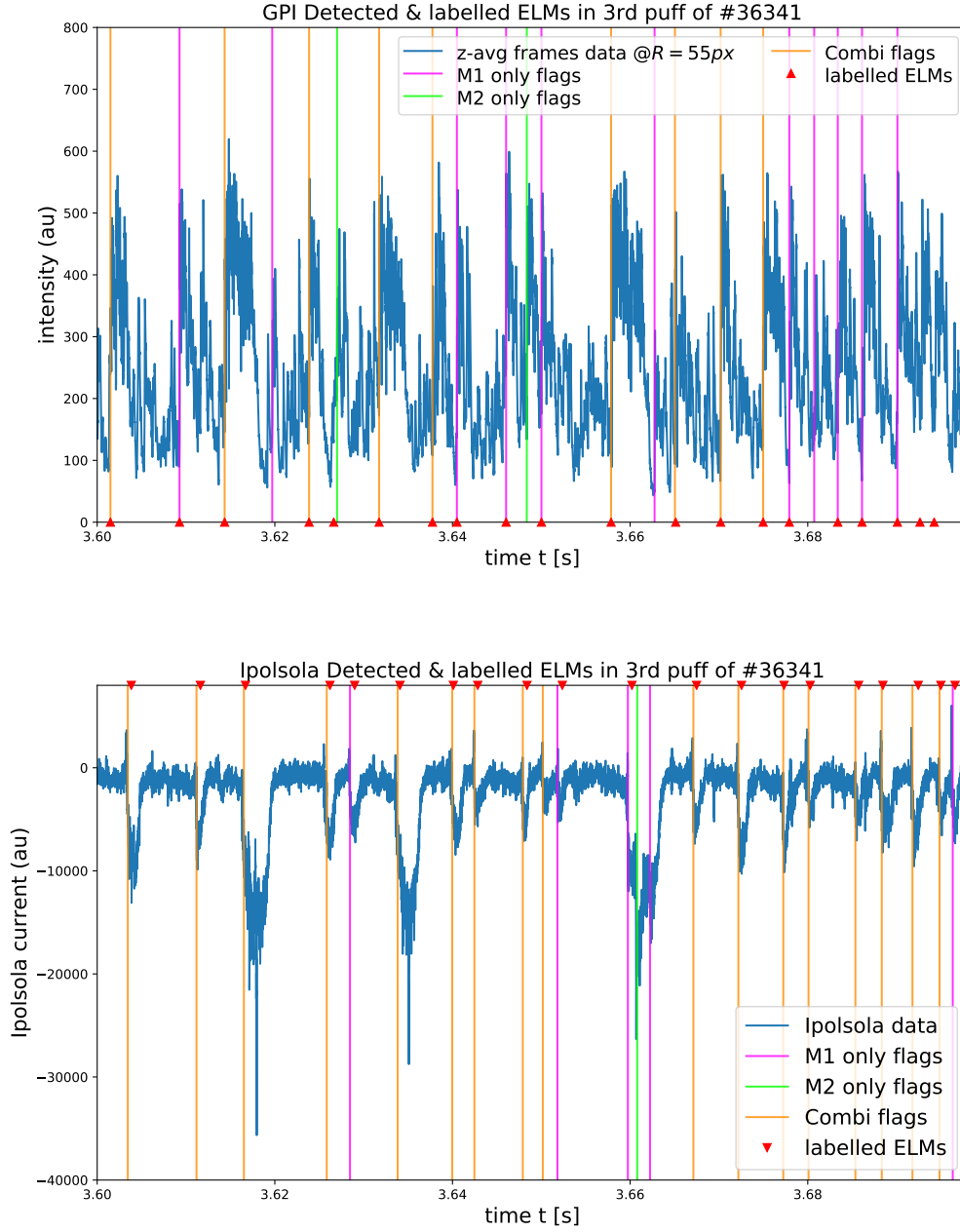


Figure 9: The labelled ELMs and the detected ELMs of the different mechanisms for the GPI (top) and Ipolsola (bottom) diagnostic. Note that this time series is only a segment of the 3rd puff of #36341.

Table 2 shows that *in the GPI*, *M1* and *M2* have similar loss values. However, the origin of the individual loss values is different. Table 2 shows that *M1* has a higher false positive rate than *M2* by 7.69 pp but a lower false negative rate than *M2* by 7.62 pp. The lower false positive rate and higher false negative



rate of M2 are reflected in the results of CM. This stems from the fact that ELMs missed by either M1 or M2 are also missed by CM, but M1 and M2 have to agree on a falsely detected ELM in order for CM to accept it.

Table 2 also shows that *M1 generally performs better than M2 in the Ipolsola*. Notice that the false positive rate of CM is higher than the false positive rate of M2. This is due to the fact that the false positive rate is not only influenced by FP but also by TP. Significantly lower TP values of CM can increase the false positive rate. However, the results in table 2 and figure 9 suggest that this effect is rather small.

It is not clear whether the differences between M1 and M2 would hold for other shots as the above results from one shot. However, it shows that *CM generally adopts the higher false negative rate and lower false positive rate of either M1 or M2*. This effect is more likely to extend to other shots: even if differences in false positive and false negative rates between M1 and M2 vary during other shots, both mechanisms still need to agree on a detected ELM. For the analysis in section 3.2 this effect is advantageous as it merely means that fewer ELMs will be included in the analysis than there were in the data. Whereas a higher false positive rate would falsely include data.

*For other purposes, such as removing ELMs from the diagnostics data, it might be more useful to accept any ELMs that were detected by either M1 or M2 or by both.* This would ensure that a minimal number of ELMs are missed in the data. Figure 9 shows the flags generated by all mechanisms against the existing labels.

## 3.2 ELM Characteristics

### 3.2.1 Temporal Shape

To create an average temporal ELM evolution CM was run on seven GPI puffs of five different shots. For the GPI (Ipolsola), 230 (210) ELMs were detected in total of which 144 (163) were detected by CM, 71 (34) by M1 only and 15 (13) by M2 only.

The mean ELM was obtained by averaging the signal at each point in time across all detected ELMs each of length  $\Delta t$ . The ELMs are extracted from the full time series of the GPI or Ipolsola diagnostic through the knowledge of  $t_i^{ELM}$  and  $t_{sample}^{ELM}$  as described in section 2.2.4. Similarly, the power normalised mean was obtained by scaling the signal at each point in time by the reciprocal of the total power  $P_i$  of the associated i-th ELM, where P is given by:

$$P_i = \sum_{t=0}^{\Delta t} (ELM_i[t])^2 \quad (21)$$

The results of the mean and power normalised mean for the GPI and Ipolsola are shown in figure 10 and 11, respectively. Figure 10 shows that the power



Figure 10: The mean (top) and power normalised mean (bottom) temporal shape of an ELM in the GPI data averaged over 144 ELMs of shots #36340, #36341, #36343, #36345 and #36346.

normalised mean ELM has a similar shape and uncertainty as the mean ELM. This implies that the included ELMs were similar in their amplitude. While the standard deviation of the mean is a better indicator of the uncertainty in amplitude, the standard deviation of the power normalised mean better represents the average shape of an ELM. As the intensity at each time is scaled by the reciprocal of the ELM power, a particularly strong ELM does

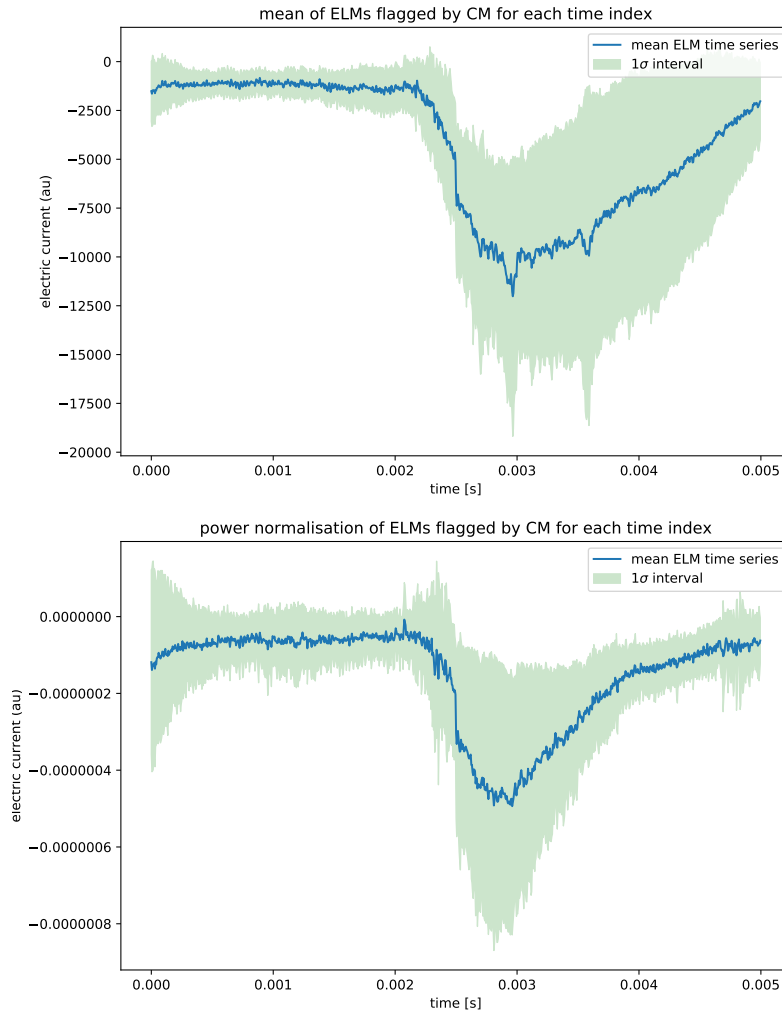


Figure 11: The mean (top) and power normalised mean (bottom) temporal shape of an ELM in the Ipolsola data averaged over 163 ELMs of shots #36340, #36341, #36343, #36345 and #36346.

not dominate in the average shape. However, as the intensities of different ELMs are each scaled by different values, the uncertainty in amplitude gets distorted.

Figure 11 shows clear differences in the shape and uncertainties of the mean ELM and power normalised mean ELM in the Ipolsola. The mean ELM shows that there is higher uncertainty in the current following the initial spike after

the beginning of the ELM for the remaining 2 ms of the ELM. This shows that the included ELMs vary more in their power than the ones included in the GPI averaging presented in figure 10. The power normalised mean ELM shows to be associated with a period of increased current of  $\sim 1$  ms. Compared to the average ELM shape in the GPI which shows an increase from the intensity before the ELM to the maximum ELM intensity on the timescale of the frame rate, the Ipolsola current rises from the current value before the ELM to the maximum current value during the ELM in  $\sim 0.5$  ms. The origin could be the differences in timescales associated with the spontaneous photon emission of the GPI and the current build up inside the divertor that causes the Ipolsola. The average ELM shapes for the GPI and Ipolsola could be used to further improve the detection mechanism M2. So far a single ELM has been used in the cross-correlation as defined in equation 16. By using the average shape in the cross-correlation of the signal, the accuracy of the mechanism could potentially increase. Knowledge of the uncertainty in amplitude at each point in time during an ELM provides further data that could be incorporated into future mechanisms.

### 3.2.2 Ipolsola and GPI Offset

An offset became apparent showing that the ELMs generally occurred later in the Ipolsola than in the GPI. The magnetic location of the GPI was averaged along the z-pixel-direction for each pixel in the R-pixel-direction. The aligned pixel  $R_a$  with the magnetic flux value closest to the average Ipolsola magnetic flux value was chosen as seen in table 3.

shot & puff no.	Ipolsola $\bar{\rho}$	GPI $R_a[px]$	GPI $\bar{\rho}(R_a)$	$\Delta\rho$
#36340 puff 2	$1.027 \pm 0.002$	22	$1.027 \pm 0.003$	$0 \pm 0.004$
#36341 puff 2	$1.026 \pm 0.002$	22	$1.027 \pm 0.003$	$0.001 \pm 0.004$
#36341 puff 3	$1.026 \pm 0.002$	22	$1.027 \pm 0.003$	$0.001 \pm 0.004$
#36343 puff 2	$1.025 \pm 0.002$	21	$1.025 \pm 0.003$	$0 \pm 0.004$
#36345 puff 2	$1.025 \pm 0.002$	21	$1.025 \pm 0.003$	$0 \pm 0.004$
#36346 puff 2	$1.026 \pm 0.002$	22	$1.027 \pm 0.003$	$0.001 \pm 0.004$
#36346 puff 3	$1.027 \pm 0.002$	22	$1.027 \pm 0.003$	$0 \pm 0.004$

Table 3: The mean magnetic location of the Ipolsola and at the aligned R-pixel-location in the GPI.

Note that the ELMs had to be detected within the GPI at  $R \sim 22$  px but M1 and M2 were developed at  $R = 55$  px where the ELM causes a sudden increase in intensity. At  $R \sim 22$  px the ratio of  $n_{neutral}$  to  $n_e$  is lower compared to  $R = 55$  px. Thus, the background plasma density exhausts the available neutral gas and an ELM does not cause a further increase in intensity. However, the

background density drops sharply after an ELM as the neutral gas atoms are ionised after the ELM occurred. This also leads to an increase in the absolute value of the first time derivative of the GPI signal. Hence, the M1 was used for this analysis.

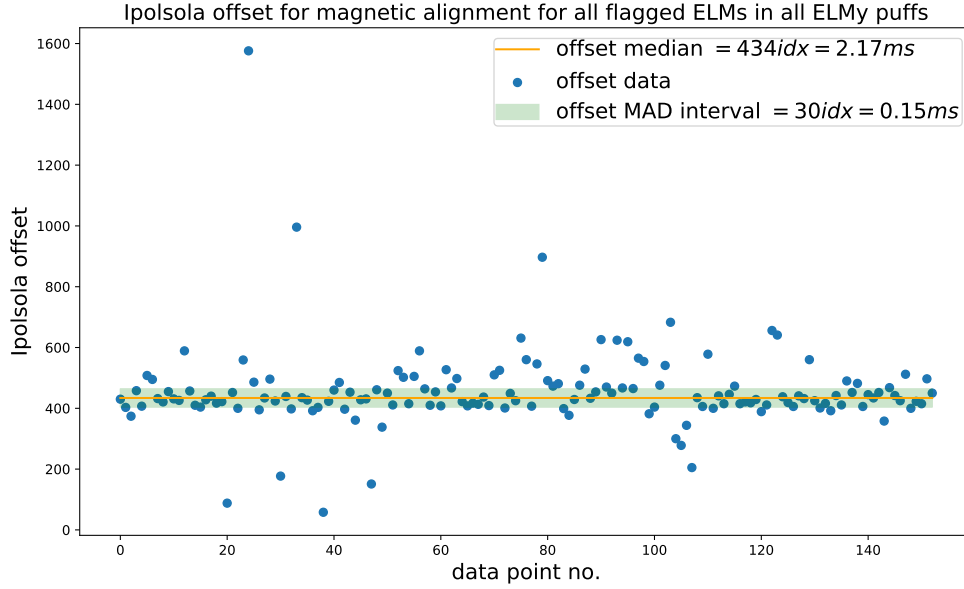


Figure 12: The GPI-Ipolsola offset for the same magnetic location for all 7 shots. The median and median absolute deviation (MAD) are used, as outliers are likely to be caused by two different ELMs as opposed to a significantly larger offset.

Figure 12 shows that there is a consistent offset between the GPI and Ipolsola of  $\Delta t = (2.17 \pm 0.15)$  ms. The  $q_{95}$  value for all shots used for figure 12 is  $q_{95} \approx 4.8$ . Studies on JET have shown that after ELMs have crossed the separatrix they tend to cause a sound wave disturbance that follows the magnetic field lines [22, p.1445]. Once triggered in the SOL at the midplane, the sound wave will reach the divertor region after completing approximately a quarter of a full poloidal transit. Using equation 4, the number of toroidal transits that are necessary to achieve  $\Delta\theta = \pi/2$  is given by:

$$N = \frac{q_{95}}{4} \quad (22)$$

Given that the toroidal circumference  $C = 2\pi R$ , the toroidal distance travelled by the ELM can be approximated as:

$$\Delta x_t = N \cdot C = \frac{\pi R q_{95}}{2} \approx 11.31 \text{ m} \quad (23)$$

with  $R \approx 1.5$  m as seen in figure 2. The poloidal distance travelled can be approximated by the distance in z-direction between the outer midplane and the divertor  $\Delta z \approx 1$  m as seen in figure 2. The total distance can then be approximated by:

$$\Delta x \approx \sqrt{(\Delta x_t)^2 + (\Delta z)^2} \approx 11.35 \text{ m} \quad (24)$$

When approximating the parallel propagation speed of the disturbance with the plasma speed of sound derived in section 2.1.3 for a typical plasma temperature of  $k_B T = 10$  keV [2], this becomes

$$C_s = \sqrt{\frac{2k_B T}{5m_p}} \approx 619 \text{ km/s} \quad (25)$$

Hence, if the sound wave disturbance follows the helical magnetic field lines, the expected delay between the GPI and Ipolsola is given by

$$\Delta t = \frac{\Delta x}{C_s} \approx 18 \mu\text{s} \quad (26)$$

The works of Manfredi *et al.* describe a delay of a few hundred microseconds between the ELM crossing the separatrix and the plasma pulse hitting the divertor plate [23, p.2]. Comparing this value and the value obtained in equation 26 to the measured median offset of  $(2.17 \pm 0.15)$  ms shown in figure 12 shows that the measured offset is at least one order of magnitude larger than expected. Thus, this offset does not seem to have a physical origin and is most likely caused by an offset in the involved clocks of the GPI and Ipolsola diagnostics.

### 3.2.3 ELM Frequency & Periodicity

Figure 13 shows the time  $\Delta t$  that passes between each successive pair of ELMs. The coefficient of variation (CV) is given by

$$c_v = \frac{\sigma}{\bar{T}_{ELM}} \quad (27)$$

The total mean ELM period is given by  $\bar{T}_{GPI} = 9.3$  ms in the GPI and  $\bar{T}_{Ipols} = 8.5$  ms in the Ipolsola. The total mean standard deviations are given by  $\sigma_{GPI} = 3.4$  ms and  $\sigma_{Ipols} = 2.5$  ms. Using equation 27, this leads to a mean coefficient of variation of 36% for the GPI and 29% for the Ipolsola. A perfectly periodic behaviour would be associated with a coefficient of variation of zero, whereas aperiodic behaviour, i.e. a uniform distribution of  $\Delta t$  would be associated with a coefficient of variation of  $1/\sqrt{3} \approx 58\%$  in the continuous limit (see appendix B for derivation). Therefore, the CV values determined for the GPI and Ipolsola confirm the quasi-periodic behaviour of ELMs stated in the works

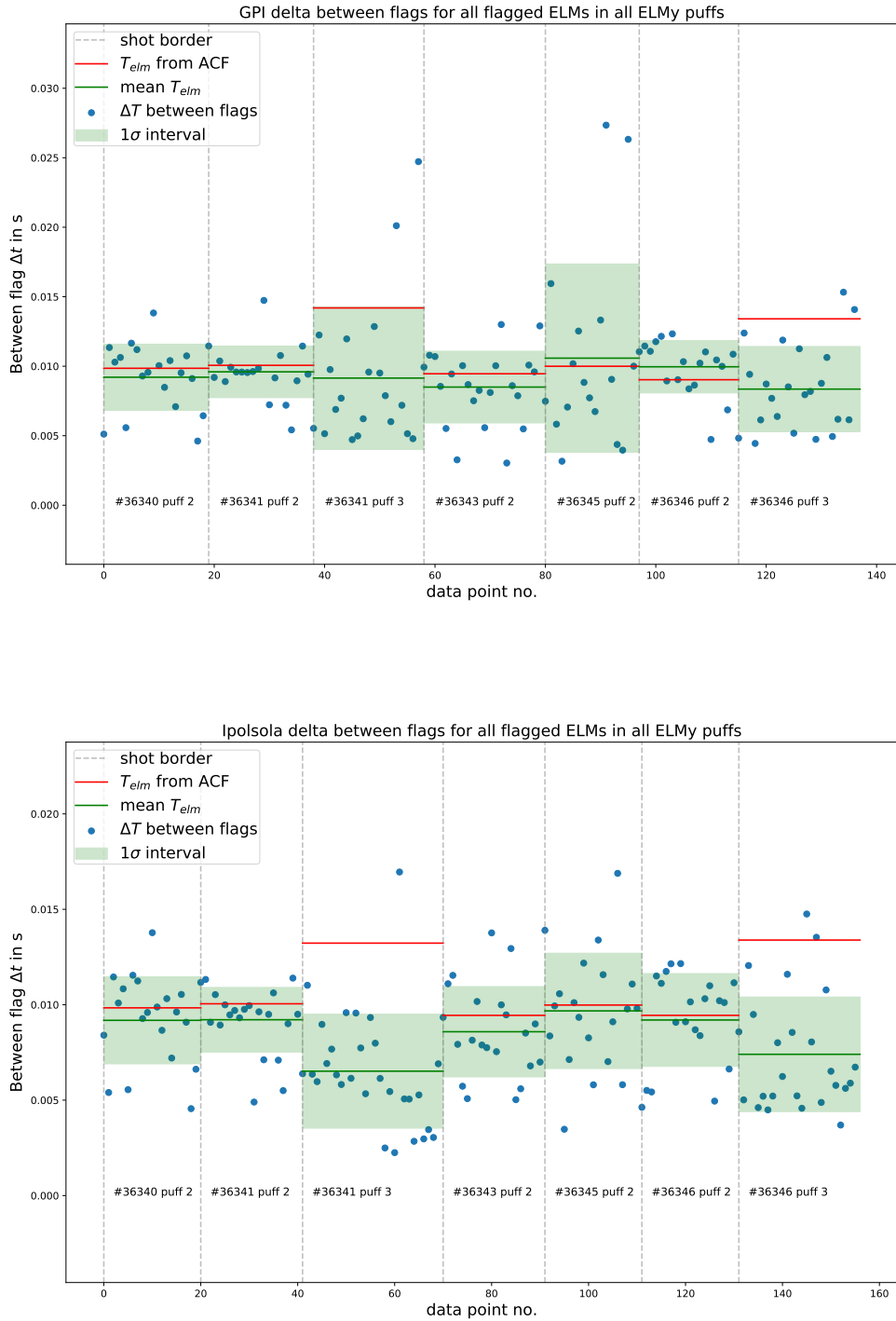


Figure 13: The time  $\Delta t$  that passes between two successive ELMs for all ELMs detected by CM for the GPI (top) and Ipolsola (bottom) diagnostic.

of Connor [24] and Keilhacker *et al.* [25].

In addition, Figure 13 shows the ELM period  $T_{ACF}$  that results from the power spectrum of the signal described in section 2.2.2. It shows that  $T_{ACF}$  is close to the mean  $T_{ELM}$  value for five of the seven puffs and lies within the  $1\sigma$ -interval for both diagnostics. For the same two puffs there is a strong deviation between  $T_{ACF}$  and  $T_{ELM}$  in both diagnostics. When looking at the data, the signal shows higher inter-ELM fluctuations [26] during these puffs possibly caused by a less stable confinement configuration. This causes more dominant frequencies in the power spectrum which could explain this deviation. However, this confirms that even though the ELMs show quasi-periodic behaviour, the method described in section 2.2.2 provides a good approximation for the mean ELM frequency in a given gas puff.

## 4 Conclusion

Two mechanisms M1 and M2 were developed to detect ELMs. M1 operates with the moving average of the signal, M2 with the cross-correlation between the signal and a single ELM. Both mechanisms were optimised and tested against a labelled shot in the GPI and Ipolsola diagnostics; M1 shows false positive (negative) rates of 11.69% (9.52%) in the GPI and 4.17% (2.86%) in the Ipolsola, whereas M2 shows false positive (negative) rates of 4% (17.14%) in the GPI and 3.23% (8.57%) in the Ipolsola. It shows that M1 generally detects more aggressive than M2. Both mechanisms were combined into a single mechanism CM that requires both M1 and M2 to detect an ELM in order to output the detection. CM shows to generally adopt the lower false positive rate but the higher false negative rate of M1 and M2.

The ELMs temporal shape was averaged over detected ELMs in seven shots, which resulted in 144 total detected ELMs in the GPI and 163 in the Ipolsola. The comparison of the mean ELM with the power normalised mean ELM shows that the detected ELMs are similarly shaped in the GPI while ELMs of different powers are detected in the Ipolsola. While the intensity in the GPI diagnostic builds up within microseconds during an ELM, the Ipolsola current rises to its maximum value in  $\sim 0.5$  ms. Following an ELM the GPI shows increased intensity values for  $\sim 3$  ms while the Ipolsola shows an average time of increased current of  $\sim 1$  ms. Future convolution based detection mechanisms could make use of the average ELM shapes and the uncertainty in amplitude at each point in time.

An apparent offset between the ELMs detected in the GPI and the ones detected in the Ipolsola shows to have a median value of  $(2.17 \pm 0.15)$  ms. Comparisons with calculations based on the ion sound speed as well as delay values described in the works of Manfredi *et al.* [23] show that this offset is not of physical origin but caused by a mismatch in the involved clocks.

A mechanism that assigns one ELM period to an entire time series of either dia-



gnostic based on the Fourier transform of the autocorrelation function shows to be a good first approximation as it lies within the standard deviation of the mean ELM period for five out of seven GPI gas puffs. The mean coefficient of variation (CV) of the time passed between two successive ELMs shows values of 36% in the GPI and 29% in the Ipolsola. As a normal distributed ELM period would lead to a CV of  $\sim 58\%$ , this confirms the quasi-periodic ELM behaviour stated in works of Connor [24] and Keilhacker *et al.* [25].

The detection mechanisms presented in this thesis provide an algorithmic basis for the development of detection mechanisms in other diagnostics such as the B-dot probe-based diagnostic [27]. In addition, they can be used for further studies of ELM characteristics such as precursor oscillations or the spatial mode structure.

# Appendices

## A Python Code

There is an interactive version of this thesis in the form of a jupyter notebook provided at [github.com/tobiasschuett/ELMs](https://github.com/tobiasschuett/ELMs) that shows the python code used in this thesis and reproduces the results.

## B Uniform Distribution

In the continuous limit the probability density function of a uniform distribution that has values different from zero between A and B is given by:

$$f(x) = \frac{1}{B - A} \quad (28)$$

with the mean given by

$$\mu = \int_{-\infty}^{\infty} f(x)x \, dx = \frac{B + A}{2} \quad (29)$$

After a rather lengthy calculation, the variance is given by [28, p.99]:

$$\sigma^2 = \langle x^2 \rangle - \mu^2 = \frac{(B - A)^2}{12} \quad (30)$$

Hence, the coefficient of variation is given by

$$c_v = \frac{\sigma}{\mu} = \frac{(B - A)/\sqrt{12}}{(B + A)/2} = \frac{B - A}{\sqrt{3}(B + A)} \quad (31)$$

In the case where  $A = 0$  this simplifies to

$$c_v = \frac{1}{\sqrt{3}} \quad (32)$$

## Acknowledgement

I would like to thank Dr. István Cziegler for supervising my work for this thesis and for providing guidance along the way. Special thanks to Steven Thomas for contributing to the work done on the Ipolsola and GPI offset, for providing figure 2 for this thesis and for giving me access to additional experimental data whenever needed. I would also like to thank the ASDEX Upgrade team for providing the experimental data for this thesis.

## References

1. Freidberg, J. P. *Plasma Physics and Fusion Energy* (Cambridge University Press, 2007).
2. Wesson, J. *Tokamaks; 4th ed.* <https://cds.cern.ch/record/1427009> (Oxford Univ. Press, Oxford, 2011).
3. Inan, U. S. & Gołkowski, M. *Principles of Plasma Physics for Engineers and Scientists* <https://www.cambridge.org/core/books/principles-of-plasma-physics-for-engineers-and-scientists/CED0992334C6F34F72EFB13EC6ADCFBA> (Cambridge University Press, 2010).
4. Rasmussen, J. J., Nielsen, A. H., Madsen, J., Naulin, V. & Xu, G. S. Numerical modeling of the transition from low to high confinement in magnetically confined plasma. *Plasma Physics and Controlled Fusion* **58**, 014031. <https://doi.org/10.1088/2F0741-3335/2F58%2F1%2F014031> (Nov. 2015).
5. Zohm, H. Edge localized modes (ELMs). *Plasma Physics and Controlled Fusion* **38**, 105–128. <https://doi.org/10.1088/0741-3335/38/2/001> (Feb. 1996).
6. Wagner, F. *et al.* Regime of Improved Confinement and High Beta in Neutral-Beam-Heated Divertor Discharges of the ASDEX Tokamak. *Phys. Rev. Lett.* **49**, 1408–1412. <https://link.aps.org/doi/10.1103/PhysRevLett.49.1408> (19 Nov. 1982).
7. Leonard, A. W. Edge-localized-modes in tokamaks. *Physics of Plasmas* **21**, 090501. eprint: <https://doi.org/10.1063/1.4894742>. <https://doi.org/10.1063/1.4894742> (2014).

8. Loarte, A. *et al.* Characteristics of type I ELM energy and particle losses in existing devices and their extrapolation to ITER. *Plasma Physics and Controlled Fusion* **45**, 1549–1569. <https://doi.org/10.1088/0741-3335/45/2F9/2F302> (Aug. 2003).
9. Biggs, S. N. Review of Progress in Understanding Edge Localised Mode Control using Resonant Magnetic Perturbations (2016).
10. Fuchert, G. *et al.* Blob properties in L- and H-mode from gas-puff imaging in ASDEX upgrade. *Plasma physics and controlled fusion* **56**, 125001. ISSN: 0741-3335. <https://iopscience.iop.org/article/10.1088/0741-3335/56/12/125001> (2014).
11. Burckhart, A. *Different ELM regimes at ASDEX Upgrade and their linear stability analysis* (Dec. 2013). <http://nbn-resolving.de/urn:nbn:de:bvb:19-164858>.
12. Cardinali, A. *et al.* Radio-frequency current drive for thermonuclear fusion reactors. *Scientific Reports* **8**, 10318. <https://doi.org/10.1038/s41598-018-27996-9> (2018).
13. Sips, A. C. C., for the Steady State Operation & the Transport Physics topical group Activity. Advanced scenarios for ITER operation. *Plasma Physics and Controlled Fusion* **47**, A19–A40. <https://doi.org/10.1088/0741-3335/47/5a/003> (Apr. 2005).
14. Piovesan, P. *et al.* Tokamak Operation with Safety Factor  $q_{95} < 2$  via Control of MHD Stability. *Phys. Rev. Lett.* **113**, 045003. <https://link.aps.org/doi/10.1103/PhysRevLett.113.045003> (4 July 2014).
15. Jiu-Xun, S., Fu-Qian, J., Qiang, W. & Ling-Cang, C. Modification to the Newton-Laplace formula of sound velocity at high pressure. *Applied Physics Letters* **89**, 121922. eprint: <https://doi.org/10.1063/1.2345596>. <https://doi.org/10.1063/1.2345596> (2006).
16. Hugh D Young, R. A. F. *University Physics with Modern Physics* (Pearson Education, 2020).
17. Harris, C. R. *et al.* Array programming with NumPy. *Nature* **585**, 357–362. <https://doi.org/10.1038/s41586-020-2649-2> (Sept. 2020).
18. Hunter, J. D. Matplotlib: A 2D graphics environment. *Computing in Science & Engineering* **9**, 90–95 (2007).
19. Virtanen, P. *et al.* SciPy 1.0: Fundamental Algorithms for Scientific Computing in Python. *Nature Methods* **17**, 261–272 (2020).
20. Chatfield, C. *The Analysis of Time Series: an Introduction (4th edition)* ISBN: 0-412-31820-2 (Chapman and Hall, 1989).
21. Olver, P. *Introduction to Partial Differential Equations* ISBN: 978-3-319-02098-3 (Jan. 2012).

22. Pitts, R. *et al.* ELM transport in the JET scrape-off layer. *Nuclear Fusion* **47**, 1437–1448. <https://doi.org/10.1088/0029-5515/47/11/005> (Oct. 2007).
23. Manfredi, G., Hirstoaga, S. & Devaux, S. Vlasov modelling of parallel transport in a tokamak scrape-off layer. *Plasma Physics and Controlled Fusion* **53**, 015012. <https://doi.org/10.1088/0741-3335/53/1/015012> (Nov. 2010).
24. Connor, J. W. Edge-localized modes - physics and theory. *Plasma Physics and Controlled Fusion* **40**, 531–542. <https://doi.org/10.1088/0741-3335/40/5/002> (May 1998).
25. Keilhacker, M. *et al.* Confinement studies in L and H-type Asdex discharges. *Plasma Physics and Controlled Fusion* **26**, 49–63. <https://doi.org/10.1088/0741-3335/26/1/003> (Jan. 1984).
26. Laggner, F., Diallo, A., Cavedon, M. & Kolen, E. Inter-ELM pedestal localized fluctuations in tokamaks: Summary of multi-machine observations. *Nuclear Materials and Energy* **19**, 479–486. ISSN: 2352-1791. <https://www.sciencedirect.com/science/article/pii/S2352179118301911> (2019).
27. Bose, S. *et al.* Understanding the working of a B-dot probe. *European Journal of Physics* **40**, 015803. <https://doi.org/10.1088/1361-6404/2018/1/015803> (Nov. 2018).
28. Abadir, K. M., Heijmans, R. D. H. & Magnus, J. R. in *Statistics* 95–148 (Cambridge University Press, 2018).